What makes lithium substituted polyacrylic acid a better binder than polyacrylic acid for silicon-graphite composite anodes?

Kevin A. Hays [a,z], Rose E. Ruther [a], Alexander J. Kukay [a], Pengfei Cao [b], Tomonori Saito [b], David L. Wood III [a], Jianlin Li [a,z]

[a] Oak Ridge National Laboratory, Energy and Transportation Science Division, Oak Ridge, TN 37831 USA

[b] Oak Ridge National Laboratory, Chemical Sciences Division, Oak Ridge, TN 37831 USA

[z] *Corresponding Author: E-mail address: hayska@ornl.gov (K. Hays);* lij4@ornl.gov *(J. Li)*

Abstract

Lithium substituted polyacrylic acid (LiPAA) has previously been demonstrated as a superior binder over polyacrylic acid (PAA) for Si anodes, but from where does this enhanced performance arise? In this study, full cells are assembled with PAA and LiPAA based Si-graphite composite anodes that dried at temperatures from 100 °C to 200 °C. The performance of full cells containing PAA based Si-graphite anodes largely depend on the secondary drying temperature, as decomposition of the binder is correlated to increased electrode moisture and a rise in cell impedance. Full cells containing LiPAA based Si-graphite composite electrodes display better Coulombic efficiency than those with PAA, because of the electrochemical reduction of the PAA binder. This is identified by attenuated total reflectance Fourier transform infrared spectrometry and observed gassing during the electrochemical reaction. Coulombic losses from the PAA and Si SEI, along with depletion of the Si capacity in the anode results in progressive underutilization of the cathode and full cell capacity loss.

Introduction

There is interest in exploring high capacity anode materials that can be paired with cathodes, such as $LiNi_xMn_yCo_zO_2$ ($x + y + z = 1$), to achieve high energy batteries. Of the potential anode materials, Si one of the most extensively researched because of its high gravimetric capacity of 3579 mAh g^{-1}, upon formation of $Li_{15}Si_4$ intermetallic.[1] Moving to Si from more conventional graphite anodes would allow for drastically lighter and thinner anodes to match the equivalent cathodes. That said, Si anodes with higher loadings have a number of issues related to large volumetric expansion accompanied by the Li alloying.[2] Dispersion of Si within a graphite matrix has proven to be an effective strategy to maximize both capacity and cycle life in these materials.[3] This method is a simple way to minimize volumetric expansion and agglomeration of the Si in a fashion that can be easily incorporated into traditional roll-to-roll manufacturing techniques.

A crucial component of these Si-graphite composite electrodes is the binder which plays an important role in particle-particle cohesion and particle-current collector adhesion. Traditionally polyvinylidene fluoride (PVDF) has been utilized for graphite based electrodes, but this binder proves ineffective with the large volumetric expansions of Si.[4] Alternatively, binders such as Na-carboxymethyl cellulose (CMC),[4] Na-alginate,[5] and poly acrylic acid (PAA) [6] show improved capabilities in Si based systems. These binders all have large quantities of hydroxyl or carboxylic acid groups that are thought to interact with the surface oxide of Si. Further improvements have been established by neutralizing the acidic protons of PAA with LiOH, forming LiPAA, with an average Li substitution of 80%.[7] Doing so may unbundle the polymer chains and possibly improve interactions with the Si surface due to the negatively charged carboxylate.[8] LiPAA has been proposed to have Li^+ conductivity, though no evidence has been produced supporting this claim.[7, 9]

LiPAA also has some undesirable features as a binder. From a mechanical standpoint PAA films are, qualitatively, more flexible than LiPAA films. We observe that 1 mm thick LiPAA films easily break when flexed between two hands, while similar PAA films can withstand more stress, though quantitative values must still be obtained. PAA also benefits from solubility in *N*-methyl-2-pyrrolidone (NMP) or water, LiPAA is only soluble in water. This is beneficial as the elimination of NMP in these slurries would allow for a more environmentally friendly means of production.[10] However, it is still unclear if water based slurries are feasible for Si, as addition of water may lead to further surface oxidation.[11, 12]

With these additional considerations in mind the question still stands: why does LiPAA perform better than PAA as a binder for Si anodes? Differences in these binders are investigated using Si-graphite composite electrodes, which are implemented in full cells with $LiNi_{0.5}Mn_{0.3}Co_{0.2}O_2$ cathodes. Secondary drying is optimized to minimize residual water while addressing degradation pathways of PAA and LiPAA. Furthermore, correlations between the electrochemical stability of these binders and the Coulombic efficiency of the related Si-graphite anodes are linked to observed gas formation.

Experimental

All chemicals were used "as received," unless otherwise noted. Li substituted polyacrylic acid (LiPAA) was produced by LiOH neutralization of polyacrylic acid (PAA, Sigma Aldrich, 450K MW). PAA was dissolved in water to ~10 wt.%. The PAA was titrated until a neutral pH was reached and stored in the refrigerator. All electrodes were fabricated at the U.S. Department of Energy Battery Manufacturing R&D facility at Oak Ridge National Laboratory. Si-graphite composite electrodes were produced with 15 wt.% Si nanoparticles (Nanoamor, 70-130 nm), 73 wt.% graphite (Hitachi, MagE 3), 2 wt.% carbon black (Imerys, C45), and 10 wt.% binder (LiPAA or PAA). LiPAA based electrodes utilized a water based slurry, while PAA based electrodes used *N*-methyl-2-pyrrolidone (NMP, Sigma-Aldrich, ≥99%). The Si was first dried under static vacuum overnight at 200 °C. Slurries were then prepared by dry mixing Si and carbon black with a planetary ball mill (Across International, PQ-N2) at 500 rpm for 10 minutes, in 500 ml zirconia jars with zirconia media. Water or NMP was added and mixed for an additional ½ hour. This Si/carbon black slurry was added to a graphite/binder slurry and mixed in a planetary mixer (Ross PDM-1/2) for 2 hours at 2500 RPM. The slurry was mixed for an additional ½ hour under active vacuum (20 mm Hg), at 1000 RPM, to remove any residual air bubbles. The solid content was ~36% by mass. The slurries were transferred and coated on 9 µm Cu foil (MTI, EQ-bccf-9u, Fig. S1) by custom slot die (Frontier Industrial Technology) to loadings of 3.4 mg cm^{-2} and 3.3 mg cm^{-2} for PAA and LiPAA based anodes, respectively.

Electrodes were punched out to 15 mm circles for coin cells (half cells) and 86.4 x 58 mm rectangles for single layer, full pouch cells. Electrodes underwent secondary drying in a vacuum oven (Napco) at a desired temperature for 18 hours under static vacuum at 25 mm Hg. Electrodes were handled in a dry room (<0.3 % relative humidity) or Ar purged glove box (Vigor Scilab) to minimize moisture exposure. Half cells were matched against Li foil (MTI, 99.9% purity 15.6 x 0.25 mm), while full cells were matched against 12.9 mg cm^{-2} $LiNi_{0.5}Mn_{0.3}Co_{0.2}O_2$ (NMC-532, Toda) cathodes (more information on the cathodes can be found in the supplementary materials). Celgard 2325 was used as separator. The electrolyte was 1.2 M $LiPF_6$ in 3:7 (w:w) ethylene carbonate (EC): ethyl methyl carbonate (EMC) (Tomiyana's High Purity

Chemicals), plus 10 wt.% fluorinated ethylene carbonate (FEC, BASF). Coin cells were flooded with electrolyte, while pouch cells were filled to 3X the total pore volume of the pouch cells (including cathode, anode and separator pores).[13, 14]

Electrochemical testing of half cells was performed on Biologic MPG-2 battery testers. Indicated C-rates are approximate. Cells were cycled at a constant temperature of 30 °C in Espec environmental chambers. Si-graphite composite half cells were discharged to 50 mV and charged to 1.5 V at C/20 for 3 cycles with 1 hour open circuit rests between each step. The rate was then increased to C/3 for 86 cycles between the same voltage limits. After this, the rate was returned to C/20 for 3 cycles, within the same voltage limits. Full cell testing was completed on Maccor series 4000 battery testers. Indicated C-rates are approximate. A tap charge was applied at C/10 to 1.5 V and held at this voltage for 15 minutes, followed by open circuit rest for 12 h. The initial 3 cycles proceeded from 3.0-4.1 V at C/20, with 1 min rests between each step. This was followed by a hybrid pulse power characterization (HPPC) test with 10 s pulses of 3C discharges and 2.25C charges. The cycling procedure continued with 97 aging cycles from 3.0-4.1 V at C/3. After aging, another HPPC test was conducted and the cells were cycled for an additional 3 cycles from 3.0 – 4.1 V at C/20.

Three electrode cells (DPM Solutions Inc.) were built with the same NMC 532 cathodes and Si-graphite composite anodes used for the full pouch cells. A $LiFePO_4$ electrode was used as a reference electrode. The electrode was coated on Al foil using 90 wt% $LiFePO_4$ (P2, Phostech Lithium Inc.), 5 wt% carbon black (Imerys C65), and 5 wt% PVDF (Solvey 5130). The electrode capacity was ~2 mAh cm^{-1}. Half cells were assembled using the $LiFePO_4$ cathodes and Li metal anodes, with 1.2M $LiPF_6$ in 3:7 EC:EMC (wt:wt) as the electrolyte. The cathode was partially delithiated to 3.4 V (50% delithiation), removed from the half cell punched out to fit the three electrode cell as a reference electrode. Respective plots were normalized to Li metal potential.

Select full pouch cells were disassembled in an Ar recirculating glovebox, after cycling as described above. 15mm circles were punched out from the cathodes and anodes, and reassembled into half cells utilizing Li metal and fresh electrolyte. Electrochemical testing and impedance spectroscopy (EIS) was performed on a Biologic VSP potentiostat. “Anode” half cells were discharged to 50 mV at C/40, while “cathode” half cells were charged to 4.2V at C/40. Cells rested for 1 h, then EIS was carried out from 200 kHz to 10 mHz, with a potential amplitude of 10 mV. Equivalent circuit fittings were performed with Biologic EC Lab, ZFit software, using the model consisting of resistive and constant phase elements (Fig. S2).

Thermogravimetric analysis (TGA) was performed on a TA Instruments Q5000 from 25 °C to 300 °C at 5 °C/min, under N_2 atmosphere. Attenuated total reflectance Fourier transform infrared spectroscopy (ATR FTIR) was performed with a Bruker Alpha spectrometer, under argon atmosphere in a glovebox. A diamond crystal was utilized with 64 averaged scans, from 350 to 4000 cm^{-1}. Base line corrections were performed within Opus software. 180° peel tests were conducted using a Mecmesin Friction Peel Tear tester with 3M 4941 double sided adhesive tape, at room temperature and at a rate of 10 mm min^{-1} over an 80 x 25.4 mm span of electrode. The documented adhesion was an average of the force over the span from 30 to 50 mm of the peel test, while the width was defined by width of the double-sided tape. Scanning electron microscopy (SEM) (Zeiss Merlin VP) was performed on electrodes before and after cycling.

Karl Fischer titration (Mettler Toledo C 20 Coulombic titrator) of the binders and electrode materials was completed using indirect extraction in chloroform to assess water content. The measurement followed equation 1, where *R* is the amount of water extracted from the electrode material in ppm, C is the amount of water extracted from the chloroform with electrode sample, B is the amount of water extracted from chloroform without the electrode material, m_{sol} is the mass of the chloroform used, and m_{ext} is the mass of the electrode sample used.

$$(1) \qquad R_{ppm} = \frac{10^6}{10^6 - C} \cdot \left(\frac{C \cdot m_{sol}}{m_{ext}} - \frac{B \cdot m_{sol}}{m_{ext}} \right)$$

Dry chloroform was stored over 3Å molecular sieves to achieve water levels undetectable by the KF titrator. Solid samples were finely ground and soaked in the chloroform for 2 days. The chloroform was extracted in a pre-weighed syringe and injected directly into the titrator.

Results and Discussion

PAA and LiPAA based Si-graphite electrodes were cycled against Li to attain relative capacities prior to full cell assembly. Details of the half cell results can be found in the supplementary material. The capacities obtained from half cell cycling were used to balance the anodes and cathodes, and obtain the negative electrode capacity to positive electrode capacity ratio (N-to-P ratio) for full cell assembly based on the initial capacities of each anode. The LiPAA based Si-graphite composite (790 ± 21 mAh g^{-1}) had an N-to-P ratio of 1.3, while the PAA composite (610 ± 117 mAh g^{-1}) was 1.1. Full cell cycling data for both composites at various secondary drying temperatures are displayed in Figure 1. For simplicity, full cells constructed with LiPAA based Si-graphite composite electrodes will be designated as “LiPAA cells”, while full cells constructed with PAA based Si-graphite composite electrodes will be designated as “PAA cells”. Furthermore, the secondary drying temperature of these anodes will be designated prior to the binder composition (e.g. 200 °C LiPAA cell is a NMC 532/ Si-graphite composite full cell, where the Si-graphite anode is made with LiPAA binder dried at 200 °C).

LiPAA cells had no detectable variation based on secondary drying temperature (Fig. 1A). The initial discharge capacity of 137 ± 3 mAh g^{-1} (per active mass of cathode) aligns well with first cycle Coulombic losses. There was a slight loss in capacity, upon increasing the rate to C/3, to 127 ± 3 mAh g^{-1} and this continued to decrease during aging to 91 ± 5 mAh g^{-1}. Returning to C/20 after 97 cycles saw an 8 mAh g^{-1} increase, comparable to the initial capacity drop and in line with the rate change.

Unlike the LiPAA cells, PAA cells displayed a trend related to the secondary drying temperature (Fig. 1B). 120 and 140 °C PAA cells performed better than those dried above these temperatures. First cycle discharge capacity ranged between 130 ± 4 and 116 ± 5 mAh g^{-1}, with electrodes dried at 160 °C being the highest and 120 °C being the lowest, though all measurements were within the error of the measurement. 160 °C PAA cells and above declined rapidly in capacity to ~75 mAh g^{-1}, before settling at 62 ± 2 mAh g^{-1} after 96 cycles, while 140 °C PAA cells and below showed a more gradual decline in capacity to 71 ± 4 mAh g^{-1}. Similar to those cells constructed with LiPAA, all PAA cells increased in capacity by 9 mAh g^{-1} upon return to C/20 from C/3 after 97 cycles.

LiPAA cells obtained first cycle Coulombic efficiencies of 84 ± 0.2%, except for the 200 °C LiPAA cells, which were slightly lower at 82 ± 6% (Fig. 1C). These cells rapidly increased to 99.6 ± 0.1% within the first 5 cycles and maintained this for 30 cycles before degrading slowly to 99.5 ± 0.1% (Fig. 1E). Upon returning the LiPAA cells to C/20, the Coulombic efficiency dropped to 98.9 ± 0.2%. PAA cells had a first cycle Coulombic efficiency of 80 ± 4%, except for 180 °C PAA cells, which were 75 ± 6% (Fig. 1D). In contrast to the LiPAA cells, the PAA cells slowly increased in Coulombic efficiency over 40 cycles to 99.6 ± 0.2% (Fig. 1F). PAA cells cycled at 140 °C and below leveled off at 99.6 ± 0.1%, while cells at 160 °C and above continued to slowly increase to 99.7 ± 0.1%. The Coulombic efficiency of all PAA cells dropped to 98.8 - 99.0% after returning to C/20.

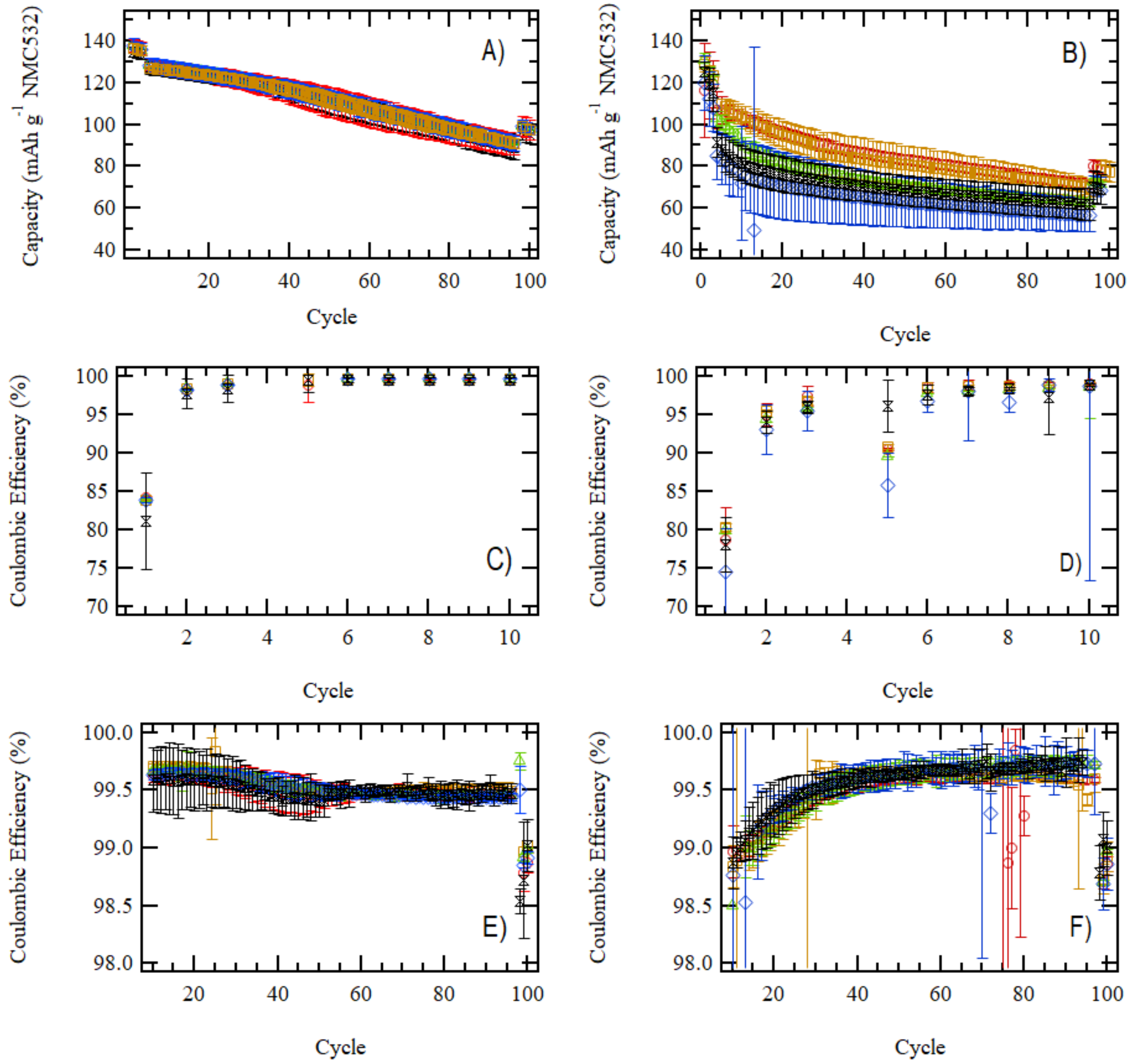

Figure 1 Cycle life of A) LiPAA full cells and B) PAA full cells. The Coulombic efficiency for the first 10 cycles of C) LiPAA full cells and D) PAA full cells. The long term Coulombic efficiency of E) LiPAA full cells and F) PAA full cells. The secondary drying temperature of the Si-graphite composite anodes are 120 °C (red circle), 140 °C (gold square), 160 °C (green triangle), 180 °C (blue diamond), and 200 °C (black hour glass). Each point is an average of 3 cells.

Hybrid pulse power characterization (HPPC) was performed after the 3rd and 96th cycles to determine changes in the overall cell impedance before and after aging cycles (Fig. S5).[15] At 50% depth of discharge (D.o.D.) LiPAA cells initially had a slightly lower impedance of ~25 Ω cm^{-2}, compared to PAA cells which were slightly higher at ~30 to 35 Ω cm^{-2} (Fig. 2). After the aging cycles, the LiPAA cells showed a small increase in impedance, independent of secondary drying temperature. By contrast, PAA cells showed higher impedance as the secondary drying temperature increased. 120 °C and 140 °C PAA cells increased slightly after cycling to values ~15 Ω cm^{-2} greater than the corresponding LiPAA cells. Above this temperature, the impedance increased greatly up to 115 Ω cm^{-2} for 200 °C PAA cells, ~3 times greater than the equivalent LiPAA cell.

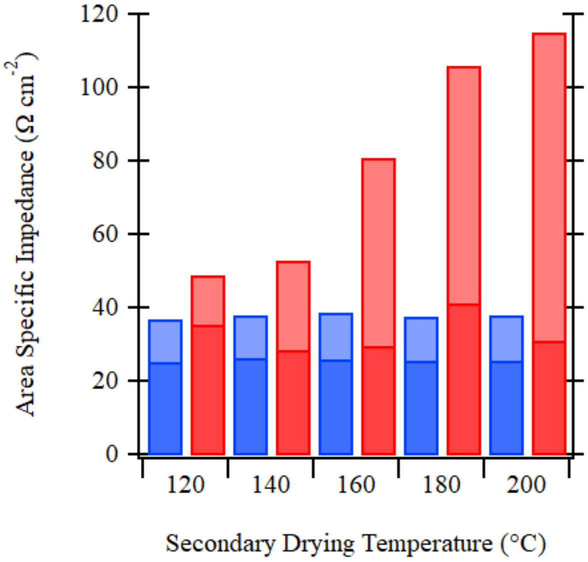

Figure 2 Area specific impedance at 50% D.o.D. of PAA based full cells (red) and LiPAA based full cells (blue) after 3 cycles (dark shading) and 96 cycles (light shading) at various secondary drying temperatures.

Impedance rise was further investigated by removing the anodes and cathodes from cycled 140 °C and 200 °C full cells, which completed the cycling protocol displayed in Figure 1. Cycled electrodes were reassembled into half-cells for electrochemical impedance spectroscopy (EIS). EIS was completed with the Si-graphite anode and NMC532 cathode half cells in a charged state (Fig. 3). The Nyquist plots of the 140 °C anodes are dominated by large depressed semicircles attributed to some combination of the charge transfer resistance (R_{ct}) and SEI resistance (R_{SEI}).[16] There is little difference in the resistance between LiPAA and PAA anodes dried at 140 °C (~ 70 Ω cm^{-2} for both PAA and LiPAA half cells). LiPAA anodes dried at 200 °C displayed a more distinct separation of these semicircles related to R_{ct} and R_{SEI}, but the sum of these contributions, $R_{\mathrm{ct}} = 59\ \Omega$ cm^{-2} and $R_{\mathrm{SEI}} = 27\ \Omega$ cm^{-2} respectively, was similar to the overall impedance of the LiPAA anodes at 140 °C. 200 °C PAA anodes indicated much larger R_{ct} and R_{SEI} values of 132 Ω cm^{-2} and 158 Ω cm^{-2}, respectively. This large jump in impedance could result from excessive SEI growth or decreased active surface area due to the particles disconnected throughout cycling. EIS from the cathodes of LiPAA and PAA full cells showed little change based on the anode selection. Resistive contributions from the cathode can be broken up into resistance from the cathode electrolyte interphase (R_{CEI}) and charge transfer resistance (R_{ct}). The resistance from the cathode was a fraction of the anode such that R_{CEI} and R_{ct} were ~14 Ω cm^{-2} for each. This EIS would indicate that the primary cause for the rise in area specific impedance (ASI) shown in Fig. 2 comes from contributions of the anodes.

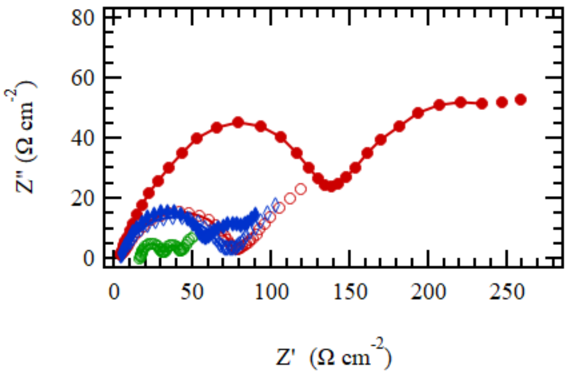

Figure 3 Nyquist plots from half cells of NMC532 cathodes (green circles), 140 °C LiPAA anodes (open blue diamonds), 200 °C LiPAA anodes (filled blue diamonds), 140 °C PAA anodes (open red circles), and 200 °C PAA anodes (filled red circles) removed from full cells after 100 cycles.

PAA full cells displayed a clear trend regarding secondary drying temperature. 120 and 140 °C PAA cells performed better than cells with anodes dried above this temperature. This may seem counterintuitive since PAA is well-known as a superabsorbent of water.[17] In contrast to the PAA, the LiPAA cell performance was independent of secondary drying temperature over the studied temperature range. The upper temperature cut-off was limited to 200 °C to avoid oxidation of the Cu foil.[18] Residual water was analyzed in PAA and LiPAA by Karl Fischer titration. As received PAA had 1.14 wt.% water, compared to LiOH titrated LiPAA (dried at 80 °C), which had only 0.03 wt.% water. TGA was used to investigate optimal temperatures to remove water from these binders (Fig. 4A). The TGA of PAA displays four distinct regions of weight loss, which are more easily identified using the first derivative (DTGA), (Fig. 4B). Though not immediately recognizable, LiPAA shares these same regions of weight loss, but with a much more gradual sloping profile. The DTGA is expanded 10X for LiPAA to identify the peaks of interest. In both binders, the first two regions of weight loss can be assigned to free water (40 °C) and adsorbed water (75 °C for LiPAA and 125 °C for PAA). In PAA, this is followed by another region of weight loss, beginning near 140 °C and reaching a maximum at 208 °C. This feature is much broader in DTGA of LiPAA, starting at 85 °C and reaching a maximum at 190 °C. This weight loss is related to the dehydration of carboxylic acid groups.[19] These neighboring carboxylic acid group will react to form an anhydride, releasing water as a byproduct (eq. 1).

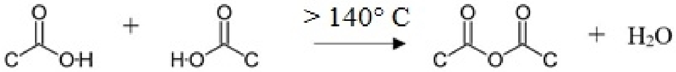

(eq. 1)

The extent of anhydride formation is less for LiPAA since 80% of the carboxylic acid groups are already substituted by carboxylate groups with Li^+ counter ions, though the onset occurs at lower temperatures. Decomposition continues at 250 °C for PAA with breakdown of the anhydride and release of CO_2, but this occurs at temperatures beyond normal electrode drying conditions. To the best of our knowledge, a detailed study of the thermal degradation of LiPAA has not been completed, but the thermal decomposition of other alkali metal polyacrylates is known. NaPAA undergoes main chain and side group scission above 400 °C, meaning these alkali metal polyacrylates should be stable under normal electrode drying conditions.[20]

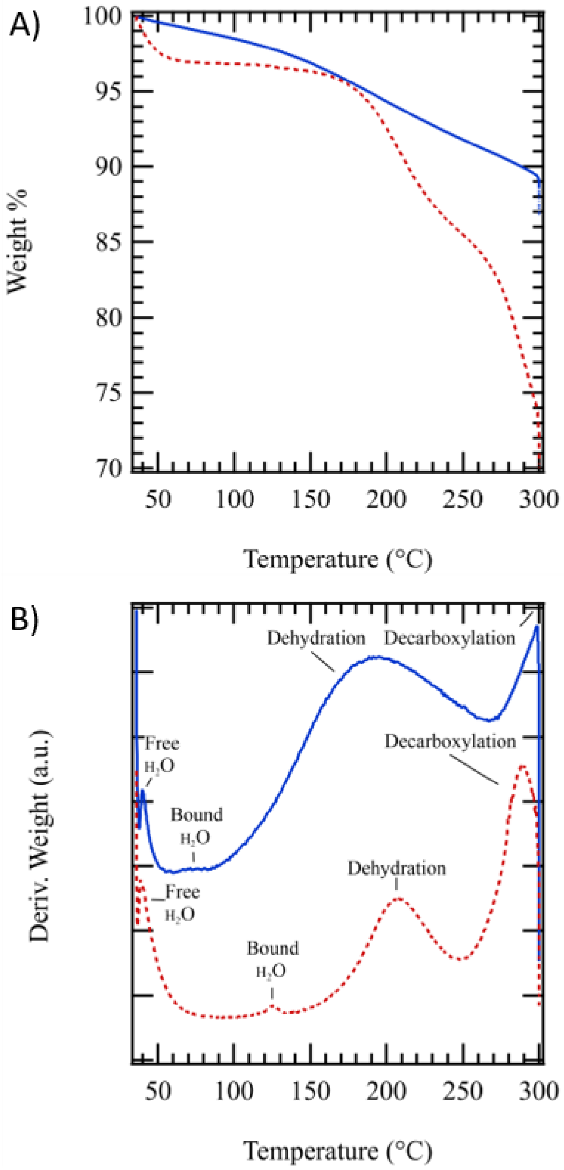

Figure 4 TGA (A) and DTGA (B) of "as received" PAA (dashed red line) and LiPAA (solid blue line). The DTGA of LiPAA was expanded 10X to more easily identify features.

The decomposition found in TGA was confirmed by ATR-FTIR (Fig. S8). A decrease in intensity of the 1706 cm^{-1} band in PAA from 120 to 200 °C is due to loss of carboxylic acid groups. This goes along with the formation of a shoulder and a band at 1802 cm^{-1} and 1012 cm^{-1}, respectively, due the formation of the anhydride. Another notable feature is the disappearance of the broad hump at ~3000 cm^{-1}, attributed to the loss of adsorbed water. For LiPAA, peaks at 1558 cm^{-1} and 1410 cm^{-1} align with the asymmetric and symmetric vibrations of carboxylate group, respectively.[21] Since the PAA is only 80% Li substituted, there is still a small peak at 1706 cm^{-1} from the residual carboxylic acid groups. Unlike PAA, there are few changes to the LiPAA spectra between 120 °C and 200 °C. The only notable difference between these spectra is a slight decrease in water band at ~3000 cm^{-1}, further indicating the temperature stability of this binder.

In PAA, the presence of the carboxylic acid group is thought to be important because of interactions between the binder and hydroxyl groups on the surface of the Si.[22, 23] These interactions are reported to come either in the form of hydrogen bonding or ester bonds between the Si and binder. ATR-FTIR results collected here show no discernable evidence of either interactions in PAA or LiPAA, as the spectra are overwhelmed by features from adsorbed species on the surface of the Si particles. It is fair to assume that the loss of these carboxylic acid groups in the PAA binder likely plays a role in the capacity fade found in 160, 180, and 200 °C PAA full cells, but this may be more a result of the mechanical properties of the PAA anodes at higher drying temperatures. The electrode adhesion of the PAA and LiPAA Si-graphite electrodes was compared at various drying temperatures, as summarized in Figure 5. The force vs extension curves can be found in Figure S9. The adhesion of the PAA electrode to the current collector dropped to ~25% of the original adhesion with increasing drying temperature. The largest drop in adhesion occurred between 140 °C and 160 °C (the onset of anhydride formation in PAA). LiPAA showed little overall change in adhesion as a function of temperature, but the adhesion of LiPAA electrodes was considerably lower than the PAA electrodes. At 120 °C PAA electrodes have adhesions that are 10 times greater than LiPAA dried at the same temperature. Such dramatic differences in the mechanics of these binders indicate there are other factors that enhance cycling capability of LiPAA electrodes. 140 °C LiPAA electrodes were calendared from 57 µm to 46 µm or 38 µm, corresponding to approximate porosities (based off wt% and density of electrode components) of 72%, 66%, and 58%, respectively. Decreasing the thickness to 38 µm improved the adhesion from 0.1 N cm^{-1} to 0.4 N cm^{-1} (ascribed to the increased contact area between the anode and Cu foil), but this also proved detrimental to the capacity of full cells made with these electrodes. Cells with LiPAA anodes calendared to 38 µm show a capacity ~5 mAh g^{-1} lower than the uncalendared electrodes (Fig. S10). Calendaring to 46 µm resulted in no capacity loss, while improving adhesion to 0.3 N cm^{-1}.

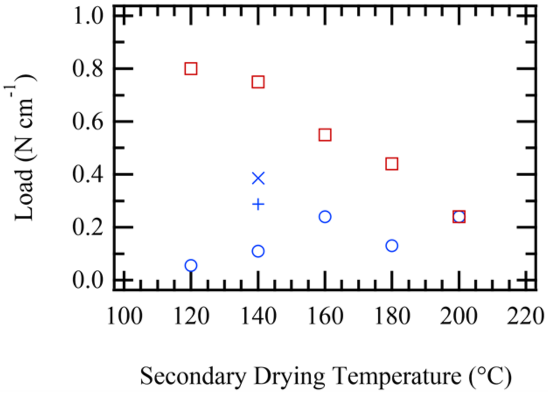

Figure 5 180° peel test of Si/graphite composite electrodes on Cu foil. Uncalendared PAA electrodes are red squares, while uncalendared LiPAA electrodes are blue circles. LiPAA electrodes were also calendared to thicknesses of 46 µm (blue +) and 38 µm (blue x) and dried at 140 °C.

In addition to thermal stability, LiPAA also shows better electrochemical stability than PAA. PAA full cells display a Coulombic efficiency ~5% worse than LiPAA cells that cannot be accounted for solely by the electrochemical reduction of additional water. The Coulombic losses continue through the first 40 cycles, summing up to a difference between the two systems of 71 mAh g^{-1} (Fig. 1C and D). Nguyen and co-workers have previously proposed the reduction of the acidic proton on the carboxylic acid of PAA to form LiPAA, following eq. 2.[24]

$$\text{–COOH} + \text{Li}^{+} + e^{-} \rightarrow \text{–COOLi} + \tfrac{1}{2}\,\text{H}_2 \qquad \text{(eq. 2)}$$

To verify these observations, PAA was mixed with 17% carbon black and coated on Cu foil. The coatings were dried at 220 °C or 120 °C, above and below the decomposition temperature of PAA. A modified pouch cell was produced with Li foil as the counter electrode and 1.2 M $LiPF_6$ in 3:7 (w:w) EC:EMC as the electrolyte. The cell was held at 1.0 V vs. Li/Li^{+} for 1 week and analyzed for gassing by the Archimedes method.[25] The PAA coating was removed, rinsed in DEC, and scraped from the Cu foil for ATR FTIR. The resulting spectra (Fig. 6) show new peaks at 1567 cm^{-1} and 1416 cm^{-1} for the 220 °C PAA sample, closely matching the asymmetric and symmetric carboxylate stretches of LiPAA. The 120 °C PAA sample also displays a change in the spectra, but with a range of peaks from 1670 cm^{-1} to 1580 cm^{-1}. While the exact reason for this is still unclear, it is recognized that the asymmetric and symmetric carboxylate stretches can vary based on the coordinating environment of the carboxylate ion.[21] The peak at 1700 cm^{-1} from the carboxylic acid stretch of PAA remains for both drying temperatures. This shows that some of the PAA remains unconverted to LiPAA, likely due to the poor electronic conductivity of the binder. This observation closely matched the gradual Coulombic efficiency gains of the PAA cells through the first 40 cycles compared to the LiPAA cells. After the 1-week voltage hold, the volume increased within the cell by 130 µl, presumably due to H_2 generation from the reduction of PAA. A more detailed gas analysis is needed to identify the content of the gassing, but the volume produced here is on the right order expected for H_2 generation based on reduction of PAA.

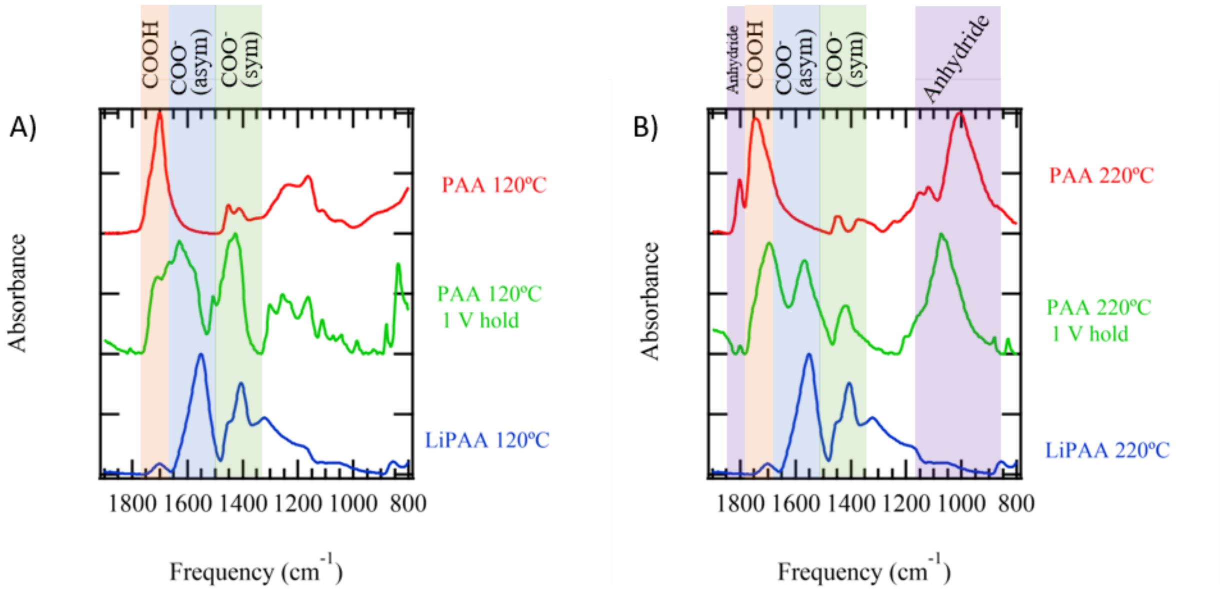

Figure 6 A) ATR FTIR spectra of PAA dried at 120 °C, PAA dried at 120 °C and electrochemically reacted with Li metal, and LiPAA dried at 120° C. B) FTIR of PAA dried at 220 °C, PAA dried at 220 °C and electrochemically reacted with Li metal, and LiPAA dried at 220 °C. The carboxylic acid stretch (COOH) is highlighted in orange, the asymmetrical carboxylate stretch (COO^- asym) is highlighted in blue, the symmetrical carboxylate stretch (COO^- sym) is highlight in green, and the Anhydride stretches are highlighted in purple.

The root cause of capacity fade was investigated using a 3-electrode cell to monitor full cell degradation over the first 36 cycles. The first and last 3 cycles were C/20, while all those in between were C/3. Cycles 4 – 33 of a 140 °C PAA cell are shown in Figure 7A, as this is where the bulk of the capacity fade was observed. The differential capacity plot of the Si-graphite anode (Fig. 7F) displays loss of capacity at 0.22 V and 0.07 V vs. Li/Li^+ during Li loading and at 0.22 V and 0.44 V vs. Li/Li^+ for Li unloading. These peaks correspond to the lithiation and delithiation of Si.[26] Peaks that match the intercalation and deintercalation of graphite do not decrease in the same fashion; instead there is an increase in the amplitude at the load voltage of

0.05 V and unload voltage of 0.13 V vs. Li/Li^+. This occurs as the Si capacity decreases, causing the anode to shift towards lower cutoff voltages and further into the graphite staging. SEM of a post-cycled PAA Si-graphite electrode shows the formation of a gossamer-like layer almost exclusively on the Si particles, which is attributed to SEI (Fig. 8). SEM of the pristine electrode is available in the supplemental material for comparison (Fig. S11).

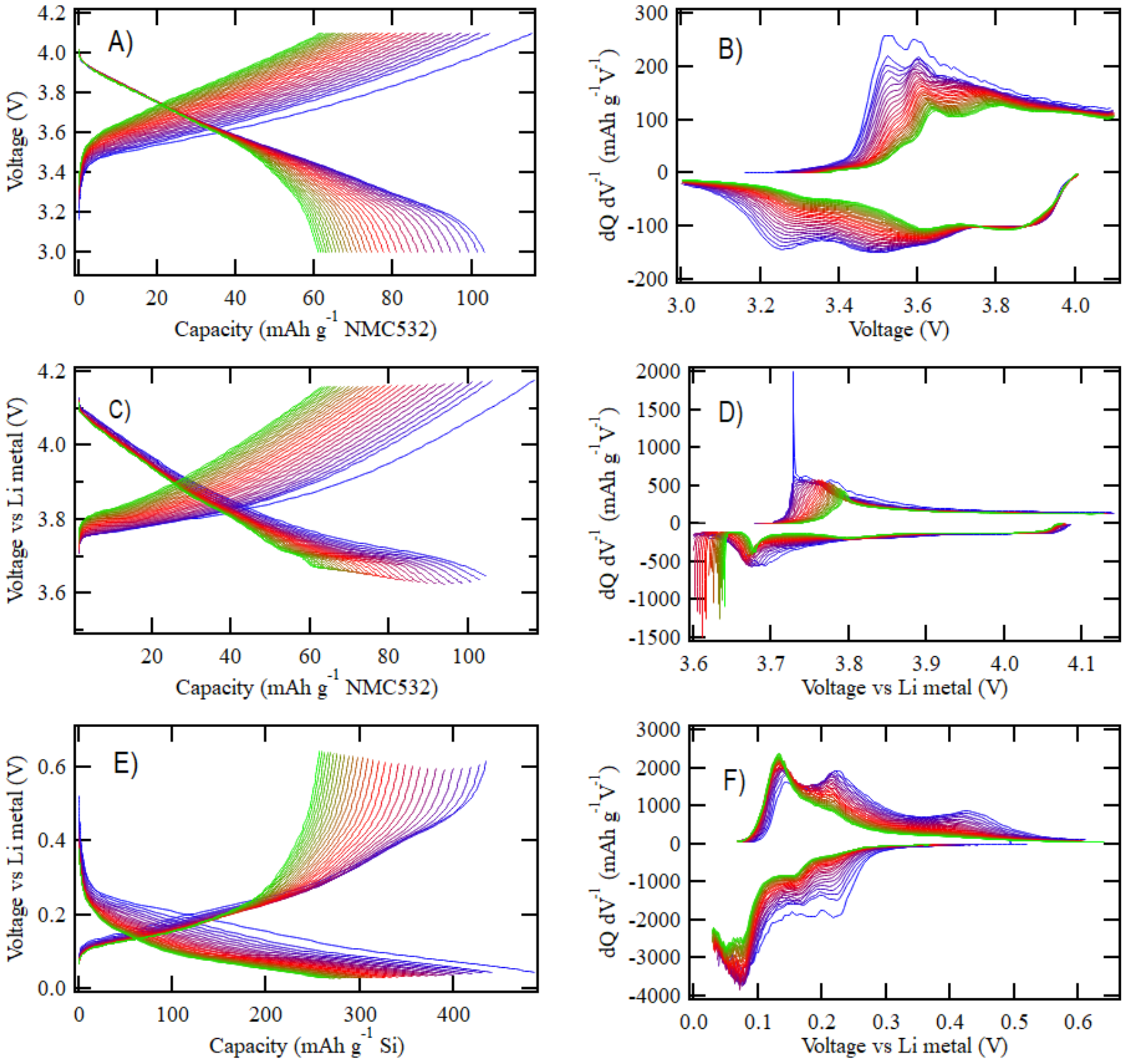

Figure 7 A) Voltage profile of NMC532-140 °C PAA Si-graphite three electrode full cell for cycles 4 – 33 at C/3 and corresponding differential capacity plot (B). C) Voltage profile of NMC532 cathode vs reference electrode and corresponding differential capacity plot (D). E) Voltage profile of 140 °C PAA Si-graphite anode vs reference electrode and corresponding differential capacity plot (F). Voltage profiles shift from blue to red to green with increasing cycles.

Capacity loss in the full cell occurs by two processes. First, a portion of the Li from the cathode is irreversibly consumed at the anode, as indicated by the Coulombic losses. Li loss in Si anodes is likely a culmination of SEI formation,[27] diffusion limited Li trapping,[28] and, in our case, reduction of the PAA binder. Once the Si becomes electrochemically isolated, rapid capacity loss occurs at the anode such that the full cell shifts from being a cathode capacity limited cell (N-to-P > 1) to an anode capacity limited cell (N-to-P < 1). On discharge of the full cell, the anode becomes delithiated sooner, causing the cell voltage to reach the lower cutoff of 3.0 V before the cathode is fully discharged (Fig. 7C). When compared to a LiPAA based 3-electrode cell, it becomes clear that LiPAA does not suffer from the same rapid capacity loss of Si found in the PAA based cell. The differential capacity plot for the LiPAA cell (Fig. S12) shows little overall change for 30 cycles, with only a small loss in the amplitude of the peaks for Li loading at 0.07 V and unloading at 0.13 V. This is reflected in full cell cycling with a much more gradual capacity fade in the early cycles of the LiPAA based cells.

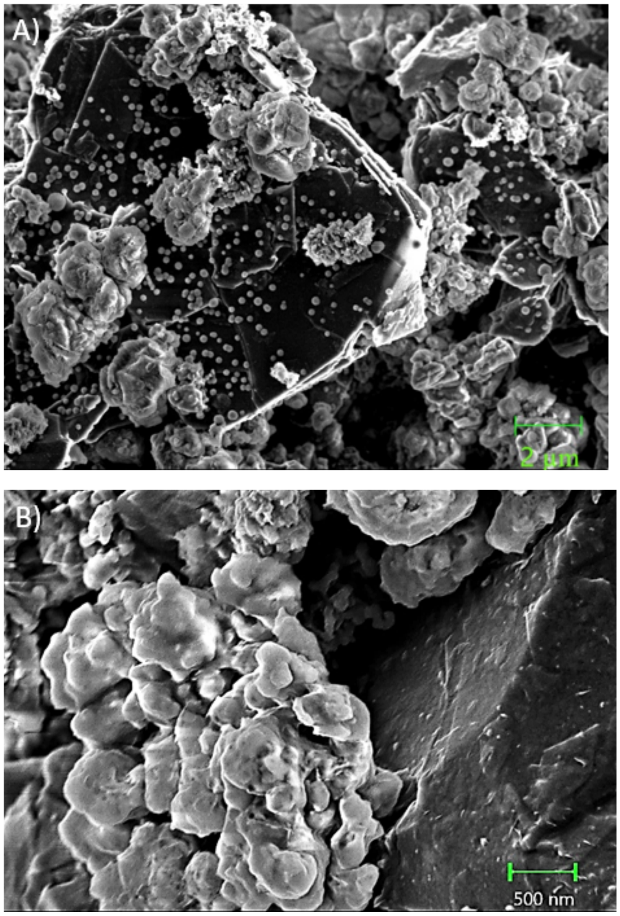

Figure 8 SEM of 140° C PAA Si-graphite anode after 100 cycles, at A) low magnification, and B) high magnification.

Electrochemical isolation of the Si in the anode increased the capacity fade of PAA full cells over LiPAA full cells. It is already clear from TGA that PAA absorbs more water than LiPAA, PAA decomposes at lower temperatures than LiPAA, and additional water is released because of this decomposition. All of these factors make residual water more difficult to remove from the PAA electrodes by secondary drying. Indirect Karl Fischer titration was utilized to investigate the water content for LiPAA and PAA electrodes dried above (160 °C) and below (120 °C) the decomposition temperature of PAA (Table 1). This method was used because thermal methods can lead to false values that overestimate residual water as a result of the PAA decomposition.

Table 1: Water content of Si-graphite composite electrode material based on indirect titration

Component	Water content 120 °C	Water content 160 °C
LiPAA Si-graphite composite anode	93 ppm	106 ppm
PAA Si-graphite composite anode	297 ppm	343 ppm
PVDF based graphite anode	107 ppm	108 ppm
NMC 532 cathode	47 ppm	-

At low drying temperatures, PAA electrodes contained ~3x more water than LiPAA electrodes. Additionally, LiPAA electrodes contained around the same amount of water as a standard graphite electrode made with polyvinylidene fluoride binder. Upon increasing the secondary drying temperature to 160 °C, the residual moisture in the PAA electrode increased by 46 ppm. This is ~3.5x greater than the water content of the LiPAA electrode, which also gained 13 ppm of water. The water content of PAA electrodes is believed to increase at 160 °C because water released during the decomposition of the PAA binder could be adsorbed on the Si surface. Si and SiO_2 particles often contain silanol groups on the surfaces forming hydrogen bonding networks with water.[29] Yoshida and co-workers demonstrated that various nano-Si powders adsorbed up to 2852 ppm of water, which was only removed after drying at 250 °C.[30] The complete decomposition of PAA should release 12,500 ppm of water. While much of this water is likely removed from the electrode by vacuum drying, a fraction remains in the electrode. Water is problematic for multiple reasons. Water can be reduced to H_2, resulting in bloating of the pouch cell. Additionally, water can hydrolyze various components of the cell, forming HF. The most obvious target of the hydrolysis is the $LiPF_6$ salt,[31] but Bareño and coworkers report that HF may be produced by reaction with silanol groups at the Si/SiO_x surface.[32] This HF destabilizes the Si SEI through corrosion of SiO_x surface species forming soluble SiF_4 or H_2SiF_6. These soluble species could be oxidized at the cathode, forming a shuttle. Based on this hypothesis, the additional trapped water in the PAA based cells could lead to the observed impedance rise and accelerated capacity loss found in this study.

Conclusion

A move towards Si-graphite composite anodes will allow for higher energy density Li ion batteries by minimizing the active anode mass, but this is not simply achieved by mixing Si with graphite. While the primary role of the binder is maintaining particle-to-particle cohesion, the choice of binder can also impact cycle life by introducing unwanted water in the cell. Here, PAA Si-graphite electrodes displayed a water content ~3.5x greater than LiPAA Si-graphite electrodes. This is despite PAA being processed in NMP, while LiPAA was processed in water. When introduced into full cells, LiPAA Si-graphite electrodes outperformed PAA Si-graphite electrodes, in part, because of the lower water content. This was likely exacerbated by the low decomposition temperature of PAA, which introduced further water back into the electrode. LiPAA does not follow the same decomposition pathway, lowering the overall water content.

Improved Coulombic efficiencies in full cells constructed with LiPAA Si-graphite electrodes are partly due to the reactivity of carboxylic acid groups. PAA has carboxylic acid groups that can be reduced to carboxylate groups at the potential of the anode, forming LiPAA and releasing H_2 gas a byproduct.

Acknowledgements

This research was conducted at Oak Ridge National Laboratory, managed by UT Battelle, LLC, for the U.S. Department of Energy (DOE) under contract DE-AC05-00OR22725. The work was sponsored by the Office of Energy Efficiency and Renewable Energy (EERE) Vehicle Technologies Office (VTO). SEM analysis was conducted at the Center for Nanophase Materials Sciences, which is a DOE Office of Science User Facility. We thank Dr. Nidia Gallego for assistance with TGA and Dr. Jagjit Nanda for use of the ATR-FTIR.

References

[1] M.T. McDowell, S.W. Lee, W.D. Nix, Y. Cui, Adv. Mater., 25 (2013) 4966-4984.

[2] L.Y. Beaulieu, K.W. Eberman, R.L. Turner, L.J. Krause, J.R. Dahn, Electrochem. Solid State Lett., 4 (2001) A137-A140.

[3] N. Dimov, S. Kugino, A. Yoshio, Journal of Power Sources, 136 (2004) 108-114.

[4] N.S. Hochgatterer, M.R. Schweiger, S. Koller, P.R. Raimann, T. Wöhrle, C. Wurm, M. Winter, Electrochemical and Solid-State Letters, 11 (2008) A76-A80.

[5] I. Kovalenko, B. Zdyrko, A. Magasinski, B. Hertzberg, Z. Milicev, R. Burtovyy, I. Luzinov, G. Yushin, Science, 334 (2011) 75-79.

[6] S. Komaba, T. Ozeki, N. Yabuuchi, K. Shimomura, Electrochemistry, 79 (2011) 6-9.

[7] J. Li, D.B. Le, P.P. Ferguson, J.R. Dahn, Electrochim. Acta, 55 (2010) 2991-2995.

[8] Z.J. Han, K. Yamagiwa, N. Yabuuchi, J.Y. Son, Y.T. Cui, H. Oji, A. Kogure, T. Harada, S. Ishikawa, Y. Aoki, S. Komaba, Physical Chemistry Chemical Physics, 17 (2015) 3783-3795.

[9] S. Komaba, K. Okushi, T. Ozeki, H. Yui, Y. Katayama, T. Miura, T. Saito, H. Groult, Electrochem. Solid State Lett., 12 (2009) A107-A110.

[10] J. Li, Z. Du, R.E. Ruther, S.J. AN, L.A. David, K. Hays, M. Wood, N.D. Phillip, Y. Sheng, C. Mao, S. Kalnaus, C. Daniel, D.L. Wood, JOM, 69 (2017) 1484-1496.

[11] A. Touidjine, M. Morcrette, M. Courty, C. Davoisne, M. Lejeune, N. Mariage, W. Porcher, D. Larcher, J. Electrochem. Soc., 162 (2015) A1466-A1475.

[12] K.A. Hays, G.M. Veith, B. Key, J. Li, Y. Sheng, D.L. Wood, Meeting Abstracts, MA2017-02 (2017) 395.

[13] S.J. An, J.L. Li, C. Daniel, H.M. Meyer, S.E. Trask, B.J. Polzin, D.L. Wood, ACS Appl. Mater. Interfaces, 9 (2017) 18799-18808.

[14] S.J. An, J. Li, D. Mohanty, C. Daniel, B.J. Polzin, J.R. Croy, S. E. Trask, D.L. Wood, J. Electrochem. Soc., 164 (2017) A1195-A1202.

[15] in: U.S.D.o.E.V.T. Program (Ed.), Idaho National Laboratory, 2014.

[16] D. Aurbach, B. Markovsky, M.D. Levi, E. Levi, A. Schechter, M. Moshkovich, Y. Cohen, Journal of Power Sources, 81-82 (1999) 95-111.

[17] F.L. Buchholz, A.T. Graham, Modern Superabsorbent Polymer Technology, Wiley-VCH, 1997.

[18] S.-K. Lee, H.-C. Hsu, W.-H. Tuan, Materials Research, 19 (2016) 51-56.

[19] I.C. McNeill, S.M.T. Sadeghi, Polym. Degrad. Stabil., 29 (1990) 233-246.

[20] I.C. McNeill, S.M.T. Sadeghi, Polym. Degrad. Stabil., 30 (1990) 213-230.

[21] G.B. Deacon, R.J. Phillips, Coordin Chem Rev, 33 (1980) 227-250.

[22] N.S. Hochgatterer, M.R. Schweiger, S. Koller, P.R. Raimann, T. Wohrle, C. Wurm, M. Winter, Electrochem. Solid State Lett., 11 (2008) A76-A80.

[23] U.S. Vogl, P.K. Das, A.Z. Weber, M. Winter, R. Kostecki, S.F. Lux, Langmuir, 30 (2014) 10299-10307.

[24] C.C. Nguyen, T. Yoon, D.M. Seo, P. Guduru, B.L. Lucht, ACS Appl. Mater. Interfaces, 8 (2016) 12211-12220.

[25] C.P. Aiken, J. Xia, D.Y.H. Wang, D.A. Stevens, S. Trussler, J.R. Dahn, J. Electrochem. Soc., 161 (2014) A1548-A1554.

[26] M.N. Obrovac, L.J. Krause, J. Electrochem. Soc., 154 (2007) A103-A108.

[27] S.E. Trask, K.Z. Pupek, J.A. Gilbert, M. Klett, B.J. Polzin, A.N. Jansen, D.P. Abraham, J. Electrochem. Soc., 163 (2016) A345-A350.

[28] D. Rehnlund, F. Lindgren, S. Bohme, T. Nordh, Y.M. Zou, J. Pettersson, U. Bexell, M. Boman, K. Edstrom, L. Nyholm, Energy & Environmental Science, 10 (2017) 1350-1357.

[29] L.T. Zhuravlev, Colloid Surface A, 173 (2000) 1-38.

[30] S. Yoshida, Y. Masuo, D. Shibata, M. Haruta, T. Doi, M. Inaba, J. Electrochem. Soc., 164 (2017) A6084-A6087.

[31] D. Aurbach, B. Markovsky, A. Shechter, Y. EinEli, H. Cohen, J. Electrochem. Soc., 143 (1996) 3809-3820.

[32] J. Bareño, I.A. Shkrob, J.A. Gilbert, M. Klett, D.P. Abraham, The Journal of Physical Chemistry C, (2017).